Available online at www.sciencedirect.com
SCIENCE DIRECT
Journal of Solid State Chemistry 179 (2006) 898–908
JOURNAL OF SOLID STATE CHEMISTRY
www.elsevier.com/locate/jssc

Phase segregation in the $Gd_{1-x}Sr_xFeO_{3-\delta}$ series

Javier Blasco*, Jolanta Stankiewicz, Joaquín García

Departamento de Física de la Materia Condensada, Instituto de Ciencia de Materiales de Aragón, CSIC-Universidad de Zaragoza, C/Pedro Cerbuna 12, 50009 Zaragoza, Spain

Received 20 July 2005; received in revised form 2 November 2005; accepted 11 December 2005
Available online 20 January 2006

Abstract

$Gd_{1-x}Sr_xFeO_{3-\delta}$ ferrites have been studied by means of X-ray powder diffraction in the whole composition range. Single-phase solid solution is found for $x<0.09$ and for $x>0.63$. At intermediate Sr content, phase segregation takes place. Compounds with $x\leqslant 0.05$ crystallize in the orthorhombic structure, space group *Pbnm*. Oxygen-deficient $Gd_{1-x}Sr_xFeO_{3-\delta}$ with $x\geqslant 2/3$ are cubic or nearly cubic. The oxygen vacancies stabilize the cubic phase for $x = 2/3$ whereas highly oxidized samples show an orthorhombic distortion, which has not been observed earlier. Magnetic and electrical properties have been measured for the single-phase solid solutions. $Gd_{1-x}Sr_xFeO_{3-\delta}$ compounds with $x\geqslant 2/3$ order antiferromagnetically below ~100 K. In the paramagnetic region, their susceptibility follows the Curie–Weiss law in all but $SrFeO_{2.96}$ compound. These ferrites show semiconducting behavior in the electrical transport likely related to atomic disorder. We find that the conductivity activation energy becomes larger by increasing either the Gd content or the oxygen vacancies.

PACS: 61.10.Nz; 61.66.Fn; 75.50.Ee; 72.15.Eb

Keywords: Ferrites; Metal–insulator transition; Miscibility gap; Perovskites; Anderson transition; Antiferromagnetism; Mixed oxides

1. Introduction

The ferrites $RE_{1-x}A_xFeO_3$ (RE = rare earth; A = alkaline earth) have attracted a considerable attention owing to their interesting physical properties [1–4]. $REFeO_3$ belongs to the family of perovskite oxides with an orthorhombic unit cell whose space group is *Pbnm* (standard group, *Pnma*) [5]. They are insulators with a strong antiferromagnetic (AF) coupling between Fe^{3+} ions. This leads to high values of the Neél temperature T_N. For instance, $T_N = 657$ K for $GdFeO_3$ [6].

On the other hand, $SrFeO_3$ is a metallic antiferromagnet with $T_N = 130$ K [7]. It exhibits a helical magnetic structure with a magnetic moment of $3.1\mu_B$ per Fe^{4+} ion [8]. It is usually assumed that Fe^{4+} ions in $SrFeO_3$ are in high spin $3d^4$ state with three localized electrons in the t_{2g} band while the fourth electron is delocalized in a broad σ^* band. This band comes from the overlap of Fe crystal-split e_g-band and O $2p$-bands [9]. Spectroscopic studies of $La_{1-x}Sr_xFeO_3$ show that the crystal field splitting is much smaller than the intra-atomic Coulomb repulsion, so Fe ions are in high spin configuration for both $LaFeO_3$ and $SrFeO_3$ [10]. These studies also revealed that the holes Sr-substituted $LaFeO_3$ are in mixed state of Fe $3d$–O $2p$ character. For low Sr content, the Fe ground state is a mixed $3d^5 + 3d^5L$ state, where L denotes a ligand hole, while mixed $3d^5L + 3d^4$ state is proposed for $SrFeO_3$ [10].

The substitution of RE with Sr in $REFeO_3$ also weakens the AF interactions. Accordingly, T_N decreases as RE content does. This is attributed to an increase of nominal Fe^{4+} ions concentration in mixed compounds that also leads to an increase of the conductivity [11]. In addition, various $RE_{1-x}A_xFeO_3$ compounds show a metal–insulator transition [2,3,12]. A charge disproportionation of Fe^{4+} into Fe^{3+} and Fe^{5+} and the consequent charge ordering of Fe^{3+} and Fe^{5+} ions is proposed in some papers to explain this transition [2,3]. Other authors use a charge density wave for it [4,13]. In any case, the existence of metal–insulator transition strongly depends on the RE size [14].

*Corresponding author. Fax: +34 97 676 12 19.
E-mail address: jbc@unizar.es (J. Blasco).

0022-4596/$ - see front matter © 2005 Elsevier Inc. All rights reserved.
doi:10.1016/j.jssc.2005.12.023

It should be mentioned that the preparation of Sr-rich samples requires strong oxidative conditions. Conventional ceramic procedures usually lead to oxygen deficient samples [15]. The oxygen vacancies reduce the coordination of some iron atoms from octahedral to square-pyramidal or tetrahedral one [11] and occasionally, the vacancies can be ordered in the lattice [16,17].

All the surveys on $RE_{1-x}Sr_xFeO_3$ mainly report results for compounds with light rare earths, in particular for $RE = La$ [11,15,18,19]. There are only few reports for $RE_{1-x}Sr_xFeO_3$ compounds with heavy rare-earths and they are devoted to samples with strong oxygen deficiency [20,21]. Nevertheless, a direct comparison between $La_{1-x}Sr_xFeO_{3-\delta}$ and $RE_{1-x}Sr_xFeO_{3-\delta}$ ($RE = Dy$, Gd) reveals some structural differences. For instance, the orthorhombic distortion, observed for $LaFeO_3$ or $PrFeO_3$ unit cells, decreases with increasing Sr content. Rhombohedral phases appear at $x \approx 0.5$–0.7 while cubic phases are found for $x \geqslant 0.8$ [18,19]. This sequence is in agreement with the trend expected from the tolerance factor of Goldschmidt. However, in Dy- or Gd-based compounds, the unit cell changes from orthorhombic to cubic at $x \approx 0.5$ and the orthorhombic distortion remains almost constant for $x \leqslant 0.5$ [20,21].

The aim of the present study is to clarify the crystal structure of the $Gd_{1-x}Sr_xFeO_{3-\delta}$ series with different oxygen stoichiometries. Since we have not found any report on the electrical or magnetic properties for this series, we also show results of magnetic susceptibility and electrical resistivity measurements for the Sr-rich single-phase compounds.

2. Experimental methods

$Gd_{1-x}Sr_xFeO_{3-\delta}$ ($x = 0$, 1/20, 1/8, 1/4, 1/3, 2/5, 1/2, 3/5, 2/3, 3/4, 7/8, 1) samples were prepared using solid-state methods. The reason to choose these compositions is two-fold. On the one hand, we are scanning the whole series and on the other hand, we are checking for the presence of charge ordered structures, which usually appear for fractional x-values. Stoichiometric amounts of Gd_2O_3, $SrCO_3$ and Fe_2O_3 were mixed, ground and calcined at 1000 °C for 1 d in air. Then, the powders were ground, pressed into pellets and sintered at 1250 °C for 1 d, also in air. The last step was repeated one more time with a final annealing at 450 °C for 10 h in the same atmosphere. Several samples were chosen after this step to test the oxygen content and crystal structure. The remaining materials were tempered at 450 °C for 1 d at high oxygen pressure (200 bars) in a Morris Research furnace.

The samples were characterized by X-ray powder diffraction using a Rigaku D-Max system. Step-scanned patterns were measured between 10° and 120° (in steps of 0.03°) at room temperature. The X-ray system was working at 40 kV and 80 mA with a counting rate of 4 s step^{-1}. We used a graphite monochromator to select the Cu$K\alpha$ radiation. The crystal structures were refined by the Rietveld method using the Fullprof package program [22].

To obtain the oxygen content, we used the method of redox titration with cerium(IV) sulfate and Mohr's salt [23,24]. Powdered samples (~100 mg) were dissolved with an excess of Mohr's salt in 3 M HCl. At this step, tetravalent Fe is reduced into Fe^{3+} by divalent irons. After heating for a few minutes, yellow solutions are obtained. A 10 mL of concentrated phosphoric acid is then added to form colorless complex of Fe^{3+}. After cooling, the excess of Fe^{2+} ions is titrated with $Ce(SO_4)_2$ solution using ferroin (one drop) as an indicator. The whole titration process is carried out under an Ar stream. The end-point is detected as a sudden change from red-orange to colorless (or very light blue) solution. This analysis was repeated three times for each sample and the standard deviation in δ is estimated to be ± 0.01.

AC magnetic susceptibility was measured between 5 and 300 K in a commercial quantum design superconducting quantum interference device (SQUID) magnetometer. Resistivity measurements were carried out using the standard six-probe AC method in the temperature range between 4 and 300 K. We checked the type of carriers using the hot probe.

3. Results

Diffraction patterns of the $Gd_{1-x}Sr_xFeO_{3-\delta}$ series show three distinct regions. The Gd-rich samples ($x = 0$ and 0.05) have the orthorhombic $GdFeO_3$ structure with lattice constants such that $b > c/\sqrt{2} > a$ (*Pbnm* space group). The Sr-rich compounds ($x \geqslant 2/3$) crystallize in cubic or pseudo-cubic structures, depending on the oxygen content. These are clearly single-phase compounds. However, the intermediate composition patterns ($1/8 \leqslant x \leqslant 3/5$) are typical of a mixture of phases. Below, we discuss in detail the main characteristics of the three regions.

3.1. Crystal structure of Gd-rich samples

$GdFeO_3$ and $Gd_{0.95}Sr_{0.05}FeO_3$ were prepared in air without the last annealing at high oxygen pressure. The samples were found to be stoichiometric within the limits of experimental error. Both compounds crystallize in the same structure with a strongly distorted orthorhombic unit cell. The distortion is brought about by the cooperative tilts of the FeO_6 octahedra in order to minimize the mismatch produced by the small size of Gd^{3+} ion [25].

The fit to X-ray data obtained for $Gd_{0.95}Sr_{0.05}FeO_3$ is shown in Fig. 1. Values of the refined parameters from the Rietveld analysis are given in Table 1 for both compositions. Our results for $GdFeO_3$ agree well with those reported earlier [5]. In $Gd_{0.95}Sr_{0.05}FeO_3$, we would expect an increase of the unit-cell volume since the Sr^{2+} ion is bigger than the Gd^{3+} one [25]. However, the unit-cell volume decreases slightly. A small decrease in the Fe–O distances (see Table 1), arising from the higher Fe valency,

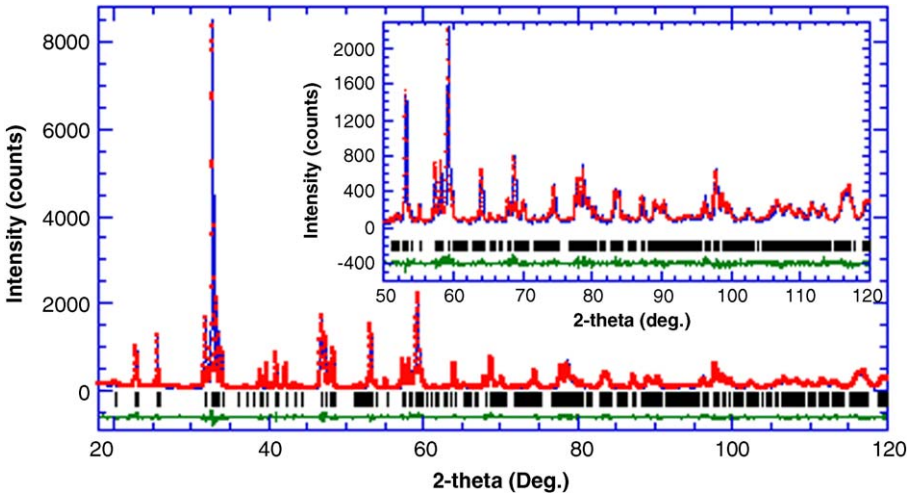

Fig. 1. X-ray refinement for $Gd_{0.95}Sr_{0.05}FeO_3$. Points and line show experimental and fit data, respectively. The difference between both sets of data is plotted at the bottom, below the tick marks of the allowed reflections. Inset: Detail of the same refinement.

Table 1
Structural parameters (space group, lattice constants, fractional coordinates, temperature factors, selected bond lengths, bond angles and reliability factors [22]) for $GdFeO_3$, $Gd_{0.95}Sr_{0.05}FeO_3$ and $Gd_{0.33}Sr_{0.67}FeO_{2.96}$

	$GdFeO_3$	$Gd_{0.95}Sr_{0.05}FeO_3$	$Gd_{1/3}Sr_{2/3}FeO_{2.96}$
Space group	*Pbnm*	*Pbnm*	*Ibmm*
a (Å)	5.3490(1)	5.3550(1)	5.4656(1)
b (Å)	5.6089(1)	5.5993(1)	5.4433(1)
c (Å)	7.6687(1)	7.6715(2)	7.6954(1)
Vol (Å^3)	230.08(1)	230.03(1)	228.95(1)
Gd: x	0.9846(2)	0.9848(2)	0.9980(4)
y	0.0629(1)	0.0609(1)	0
B (Å^2)	0.19(3)	0.18(2)	0.48(2)
Fe: B (Å^2)	0.10(5)	0.17(4)	0.10(2)
O1: x	0.1116(14)	0.1087(15)	0.4601(10)
y	0.4569(14)	0.4573(15)	0
B (Å^2)	0.77(10)	0.68(11)	0.75(7)
O2: x	0.6960(11)	0.7006(12)	$\frac{1}{4}$
y	0.3021(11)	0.2994(12)	$\frac{1}{4}$
z	0.0521(9)	0.0525(8)	0.5242(11)
B (Å^2)	0.77(10)	0.68(11)	0.75(7)
Fe–O1 (Å) × 2	2.022(3)	2.018(3)	1.936(1)
Fe–O2 (Å) × 2	2.032(6)	2.031(6)	1.937(1)
Fe–O2 (Å) × 2	2.009(6)	1.999(6)	1.937(1)
Fe–O1–Fe (deg)	142.9(1)	143.6(1)	167.1(1)
Fe–O2–Fe (deg) × 2	147.1(2)	148.0(2)	168.9(1)
R_{wp}/R_{Bragg}	9.5/4.6	8.8/3.4	7.6/3.8

Atoms are located in the *Pbnm* (*Ibmm*) space group as follows: Gd/Sr at 4c: $x\,y\,\frac{1}{4}$ (4e: $x\,0\,\frac{1}{4}$); Fe at 4b: $\frac{1}{2}\,0\,0$ (4b:$\frac{1}{2}\,0\,0$); O1 at 4c: $x\,y\,\frac{1}{4}$ (4e: $x\,0\,\frac{1}{4}$); O2 at 8d: $x\,y\,z$ (8*g*: $\frac{1}{4}\,\frac{1}{4}\,z$). Numbers in parenthesis refer to standard deviation of the last significant digits.

may be responsible for such behavior. In addition, the size mismatch and the orthorhombic distortion in the *ab*-plane are smaller for $x = 0.05$. The orthorhombic distortion is defined as $|\mathbf{a}-\mathbf{b}|/(\mathbf{a}+\mathbf{b})$, where **a** and **b** are the crystal axes. It equals to 2.4×10^{-2} and 2.2×10^{-2} for $GdFeO_3$ and $Gd_{0.95}Sr_{0.05}FeO_3$, respectively. Along with the decrease of the orthorhombic distortion, we note an increase of the Fe–O–Fe bond angles for the $Gd_{0.95}Sr_{0.05}FeO_3$ sample.

3.2. Crystal structure of Sr-rich samples

Two sets of $Gd_{1-x}Sr_xFeO_{3-\delta}$ samples with a nominal composition of $x \geqslant 2/3$ were studied. One set was annealed at high oxygen pressure and, consequently, shows only a slight oxygen deficiency. The samples of the second set were sintered in air and have larger concentration of oxygen vacancies. For $x = 1$, oxygenated samples have a nominal composition of $SrFeO_{2.96}$, in agreement with previous reports on samples prepared under similar conditions [18]. Their crystal structure is cubic with space group $Pm\bar{3}m$ [16]. Samples sintered in air show $\delta \sim 0.14$. Their X-ray patterns exhibit superstructure peaks typical of the $Sr_8Fe_8O_{23}$ compound whose structure has been reported recently [16].

The oxygenated $x = 7/8$ and $x = 3/4$ samples are slightly oxygen deficient as well. We find $\delta = 0.05$ and 0.04 for $x = 7/8$ and 3/4, respectively. The crystal cell is cubic in both compounds, as it is in $SrFeO_{2.96}$. The $x = 3/4$ sample prepared in air has larger concentration of oxygen vacancies ($\delta = 0.13$). However, its crystal structure is also cubic. No superstructure peaks are observed in the X-ray pattern suggesting a random distribution of oxygen vacancies through the crystal.

The compound with $x = 2/3$, synthesized in air, has a composition $Gd_{1/3}Sr_{2/3}FeO_{2.90}$. It also crystallizes in a cubic structure as can be seen in Fig. 2a. We obtain excellent fits to the X-ray patterns using the $Pm\bar{3}m$ space group. Data for other compounds with the cubic phase can be fitted equally well. The refined parameters for these compounds are given in Table 2. We note that the size of the unit cell depends mainly on the oxidation state of Fe atoms in the FeO_6 octahedron. Other factors like the Gd/Sr ratio (Gd^{3+} is smaller than Sr^{2+} [25]) or the concentration

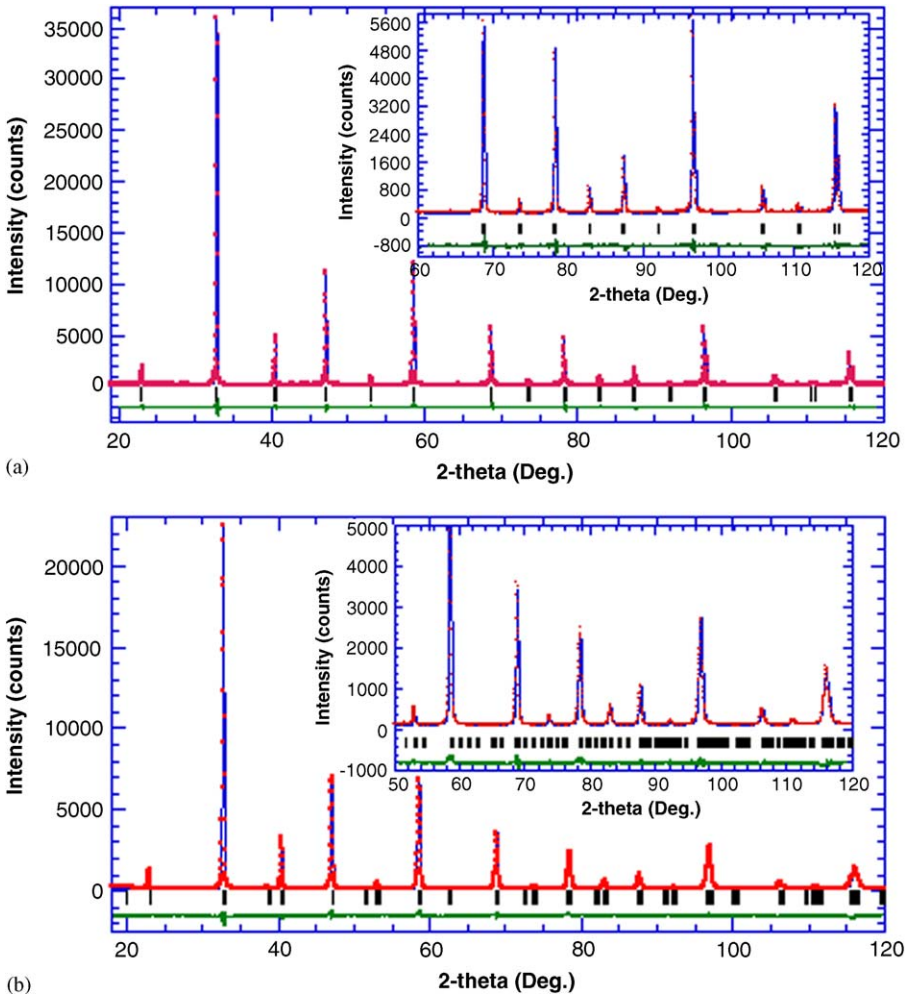

Fig. 2. X-ray refinement for (a) $Gd_{1/3}Sr_{2/3}FeO_{2.90}$ and (b) $Gd_{1/3}Sr_{2/3}FeO_{2.96}$. Points and lines have the same meaning as in Fig. 1. Insets: Details of the same refinements at high angles.

Table 2
Lattice parameters, Fe^{4+} content, temperature factors and reliability factors [22] for the cubic samples of the $Gd_{1-x}Sr_xFeO_{3-\delta}$ series with $x \geqslant 2/3$

	$Gd_{1/3}Sr_{2/3}FeO_{2.90}$	$Gd_{1/4}Sr_{3/4}FeO_{2.87}$	$Gd_{1/4}Sr_{3/4}FeO_{2.94}$	$Gd_{1/8}Sr_{7/8}FeO_{2.95}$	$SrFeO_{2.96}$
a (Å)	3.8654(1)	3.8665(1)	3.8582(1)	3.8529(1)	3.8531(1)
Fe^{4+} (%)	47	49	63	74	92
Gd/Sr: B (Å^2)	0.59(4)	0.22(4)	0.53(2)	0.39(2)	0.47(2)
Fe: B (Å^2)	0.08(5)	0.06(3)	0.08(2)	0.09(2)	0.31(3)
O: B (Å^2)	1.42(12)	1.48(10)	1.55(9)	0.93(6)	0.57(6)
R_{wp}/R_{Bragg}	9.0/3.3	9.3/4.0	8.9/3.1	8.2/3.2	9.5/3.6
χ^2	2.7	1.9	3.2	2.9	3.0

Gd/Sr is located at (1b): $\frac{1}{2}\frac{1}{2}\frac{1}{2}$; Fe at (1a):0 0 0; O at (3d): $\frac{1}{2}$ 0 0. Numbers in parenthesis refer to standard deviation of the last significant digits.

of oxygen vacancies are less important. Generally, larger unit cell corresponds to lower Fe oxidation state (see Table 2).

The $x = 2/3$ sample, annealed under an oxygen pressure of 200 bars, has a nominal composition of $Gd_{1/3}Sr_{2/3}FeO_{2.96}$. Splitting of certain diffraction peaks in its X-ray pattern indicates that the unit cell is not a simple cubic one. The assignment of the cell type for this pseudo-cubic phase is not easy. After probing various structural models, we found three alternative explanations for the observed pattern. They are based on the $I2/a$ (No. 15), *Pbnm* (No. 62) and *Ibmm* (No. 74) space groups and differ in the tilts of the FeO_6 octahedra. Using the Glazer's terminology [26], the tilting schemes are $a^-b^-b^-$, $a^0b^-b^-$, and $a^+b^-b^-$ for $I2/a$, *Ibmm*, and *Pbnm* space groups, respectively. The atomic coordinates for them are given in

Ref. [27]. It is noteworthy that all three models give accurate refinements of the patterns with good reliability factors (R_{Bragg} below 5%). Taking into account that (i) there are no superstructure reflections in the pattern from a^+ or a^- tilts; (ii) the fractional atomic coordinates of some (in particular oxygen) atoms show large standard deviations for *Pbnm* and *I*2/*a* space groups; and (iii) *Pbnm* and *I*2/*a* models yield highly distorted FeO_6 octahedra with unusual large and short Fe–O distances, we conclude that the unit cell of $Gd_{1/3}Sr_{2/3}FeO_{2.96}$ corresponds to the *Ibmm* space group. Moreover, such assignment also shows the best reliability factors. For instance, R_{Bragg} is 3.2, 4.7 and 4.9 for *Ibmm*, *Pbnm* and *I*2/*m* models, respectively.

The best fit is shown in Fig. 2b and the values of the refined parameters are given in Table 1. We find quite regular FeO_6 octahedra in $Gd_{1/3}Sr_{2/3}FeO_{2.96}$ with Fe–O distances close to those obtained for the cubic phase. The Fe–O–Fe bond angles are smaller than 180° but larger than in $GdFeO_3$. It is interesting to compare $GdFeO_3$ and $Gd_{1/3}Sr_{2/3}FeO_{2.96}$. Although both compounds are orthorhombic, they exhibit different tilts of FeO_6 octahedra [26], which can be understood in terms of the tolerance factor of Goldschmidt [28]. This factor is defined in this case as $t = RE{-}O \times 2^{-1/2} \times Fe{-}O^{-1}$, where *RE*–O and Fe–O stand for the respective inter-atomic distances. Cubic cells are found for $t \sim 1$ and cells with lower symmetries are observed for $t < 1$. From the data of Tables 1 and 2, it is easy to see that t approaches 1 as Sr content increases. Upon increasing t, the usual trend in $A^{3+}B^{3+}O_3$ perovskites is orthorhombic (*Pbnm*)→rhombohedral ($R\bar{3}c$)→cubic ($Pm\bar{3}m$). Since the occurrence of $R\bar{3}c$ cells in $A^{2+}B^{4+}O_3$ perovskites is rare [29], we would expect cubic structure for Sr-rich compounds. Indeed, we find that $Gd_{1/3}Sr_{2/3}FeO_{2.96}$ is nearly cubic with $\mathbf{a} > \mathbf{b} \sim \mathbf{c}/\sqrt{2}$. The orthorhombic strain in this compound is approximately 2×10^{-3}, one order of magnitude lower than in $GdFeO_3$ or $Gd_{0.95}Sr_{0.05}FeO_3$. This finding suggest that the elastic strain produced by the size mismatch between Sr^{2+} and Gd^{3+} is better stabilized in the *Ibmm* cell than in rhombohedral or tetragonal lattices. To the best of our knowledge, $Gd_{1/3}Sr_{2/3}FeO_{2.96}$ is the first case of orthoferrite crystallizing in the *Ibmm* structure though there are several manganites [30,31] and Bi-based perovskites [32] whose structure belongs to this space group.

To see how the oxygen content affects crystal structure we compare the two $x = 2/3$ compounds. The oxygen-deficient $Gd_{1/3}Sr_{2/3}FeO_{2.90}$ is cubic while the more stoichiometric $Gd_{1/3}Sr_{2/3}FeO_{2.96}$ is orthorhombic. Oxygen vacancies, randomly distributed in the lattice, seem to favor a cubic structure.

3.3. Crystal structure for intermediate compositions

At first glance, the diffraction patterns of compounds with $1/8 \leqslant x \leqslant 3/5$ (see Fig. 3) show features typical of a $GdFeO_3$ structure as reported in Ref. [20]. However, we observe that (i) intensity of superstructure peaks decreases, without changing their positions, as x increases; (ii) peaks, which are characteristic of the $Gd_{1/3}Sr_{2/3}FeO_{2.96}$ compound, grow up with increasing x. These observations seem to point out to the presence of a miscibility gap with phase segregation in $Gd_{1-x}Sr_xFeO_{3-\delta}$ system. The Rietveld analysis of the X-ray patterns gives more support to this conclusion. Fig. 4a shows the refinement of the nominal $Gd_{2/3}Sr_{1/3}FeO_{2.98}$ composition using a single $GdFeO_3$-like phase. The agreement between experimental and calculated patterns is very poor. Excellent fits are obtained however when two phases are used as exhibited in Fig. 4b. Both phases belong to the perovskite family. One of them is a $GdFeO_3$-type and the second one is a pseudo-cubic phase. Their structures are like that observed for $Gd_{0.95}Sr_{0.05}FeO_3$ and for $Gd_{1/3}Sr_{2/3}FeO_{2.96}$ (see Table 1), respectively. We obtain similar results for other $1/8 \leqslant x \leqslant 3/5$ samples. Quantitative analysis shows that each phase follows a

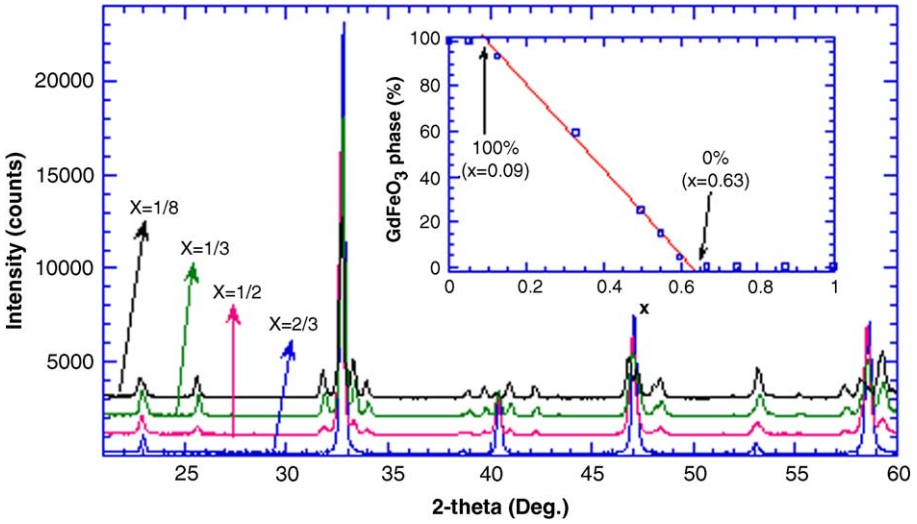

Fig. 3. X-ray patterns for $Gd_{1-x}Sr_xFeO_{3-\delta}$ ($x = 1/8$, 1/3, 1/2 and 2/3). Inset: Content (in %) of the $GdFeO_3$-like phase in the $Gd_{1-x}Sr_xFeO_{3-\delta}$ samples. The straight line is a linear fit to the data for $1/3 \leqslant x \leqslant 0.6$ samples.

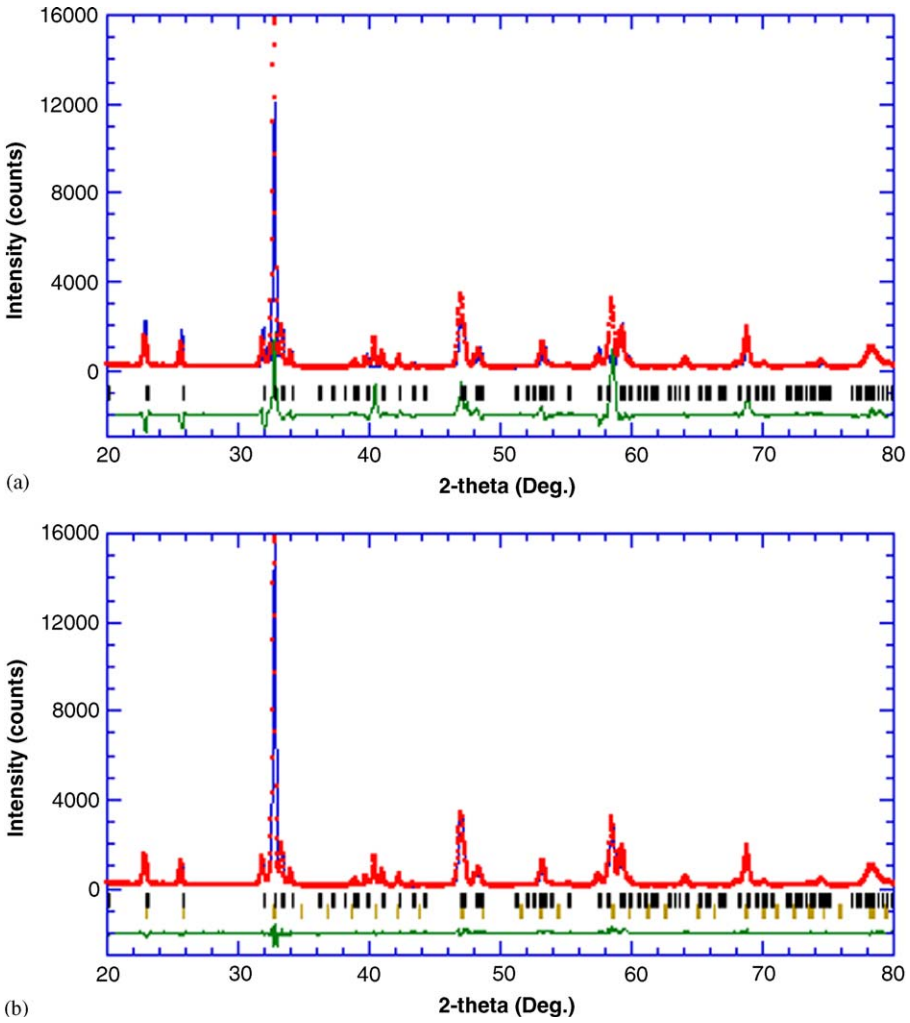

Fig. 4. (a) One-phase refinement for the $Gd_{2/3}Sr_{1/3}FeO_{3-\delta}$ sample with a $GdFeO_3$-like phase. Point and lines have the same meaning as in Fig. 1. (b) Two-phase refinement for the same sample. The first and second row of tick marks belong to the $GdFeO_3$-like and $Gd_{1/3}Sr_{2/3}FeO_{2.96}$-like phases, respectively.

lever rule. This is shown in the inset of Fig. 3 for the $GdFeO_3$-like phase. Linear extrapolation yields the limits for the miscibility gap which agree with the finding of single phases for $x = 0.05$ and $x = 2/3$ compounds.

We find the same results for samples prepared in air (not shown here). In this case, an orthorhombic $GdFeO_3$ and a cubic $Gd_{1/3}Sr_{2/3}FeO_{2.9}$-like are the two phases within the miscibility gap. The limits of the gap remain alike.

3.4. Magnetic properties

Temperature variation of AC magnetic susceptibility, χ', versus temperature has been measured for all single-phase compounds with $x \geqslant 2/3$. Fig. 5 shows obtained data for various samples. For $SrFeO_{2.96}$, $\chi'(T)$ peaks at approximately 125 K as this compound orders antiferromagnetically below this temperature [7–9]. The $Gd_{1/8}Sr_{7/8}FeO_{2.94}$ also exhibits a peak in its susceptibility curve at 72 K. The large Gd^{3+} paramagnetic signal hinders the direct observation of iron ordering in samples with higher Gd content. However, such ordering can be inferred from two features, which are shown in the inset of Fig. 5 for the $Gd_{1/4}Sr_{3/4}FeO_{2.94}$. First of all, a kink in the $1/\chi'(T)$ curves is clearly visible at low temperatures for these compounds. Secondly, the out-of-phase component of the AC susceptibility exhibits a sharp rise at the same temperature. This fact is often observed at T_N in semiconducting ferrites [33] and can be attributed to a small spin canting in the antiferromagnetically ordered state [14]. Therefore, it is quite likely that the observed features are hallmarks of AF ordering in semiconducting $Gd_{1-x}Sr_xFeO_{3-\delta}$ samples. Estimated T_N values are given in Table 3. Our results agree with previously reported values of T_N for $Gd_{1/3}Sr_{2/3}FeO_3$ [14] and $SrFeO_3$ [7].

For $T > T_N$, $1/\chi'(T)$ varies linearly with T for all samples (see inset of Fig. 5) but $SrFeO_{2.96}$. We fit the Curie–Weiss law, $\chi' = C/(T-\theta)$, to the AC magnetic susceptibilities data between 150 and 300 K. Here, C and θ are the Curie and Weiss constants, respectively. The best values of fitting parameters are given in Table 3. The inset of Fig. 5 shows the obtained fit for $Gd_{1/4}Sr_{3/4}FeO_{2.94}$. Overall, all compositions show effective paramagnetic moments that are close

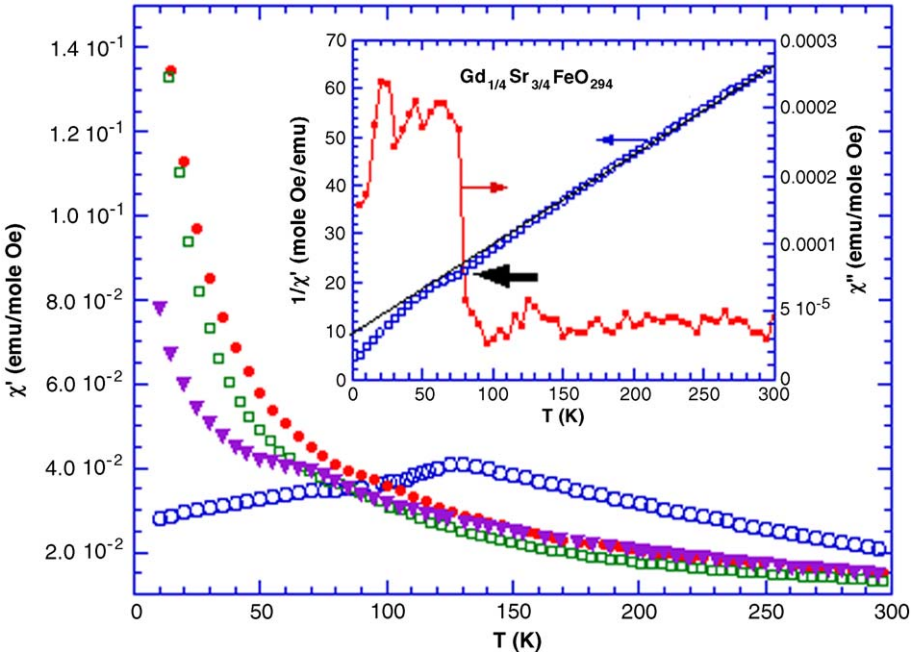

Fig. 5. The in-phase AC magnetic susceptibility for $SrFeO_{2.96}$ (white circles), $Gd_{1/8}Sr_{7/8}FeO_{2.95}$ (triangles), $Gd_{1/4}Sr_{3/4}FeO_{2.87}$ (squares) and $Gd_{1/3}Sr_{2/3}FeO_{2.96}$ (black circles). Inset: Inverse of the in-phase and out-of-phase components of the AC magnetic susceptibility for the $Gd_{1/4}Sr_{3/4}FeO_{2.94}$ sample. The straight line represents the fit to the Curie–Weiss law. Broad arrow indicates the kink in the $1/\chi'$ curve.

Table 3
Magnetic constants obtained by fitting the Curie–Weiss law to the in-phase AC magnetic susceptibility

	C (emu K/mol)	ρ_{eff} (μ_B)	ρ_{th} (μ_B)	θ (K)	T_N (K)
$Gd_{1/3}Sr_{2/3}FeO_{2.96}$	5.35	6.55	7.0	−61	98
$Gd_{1/3}Sr_{2/3}FeO_{2.90}$	6.57	7.25	7.1	−126	96
$Gd_{1/4}Sr_{3/4}FeO_{2.87}$	5.15	6.4	6.7	−94	90
$Gd_{1/4}Sr_{3/4}FeO_{2.94}$	5.36	6.55	6.6	−47	76
$Gd_{1/8}Sr_{7/8}FeO_{2.95}$	5.02	6.3	5.9	−77	72
$SrFeO_{2.96}$	5.29	6.5	4.95	+43	125

The fitting range is $150 \leqslant T \leqslant 300$ K in all samples but $SrFeO_{2.96}$ where it is $235 \leqslant T \leqslant 300$ K.

to the calculated ones, taking into account the contributions from Gd^{3+} ions and from the nominal mixture of Fe^{3+} and Fe^{4+} (spin-only) ions. We obtain negative values of θ, as expected for AF ordering. For $x = 2/3$ and 3/4 compositions, $|\theta|$ increases with increasing concentration of nominal Fe^{3+} ions. Such behavior, also found for T_N in related series, has been attributed to the large exchange coupling of Fe^{3+} ions [15]. However, in our case the $x = 7/8$ sample has an unexpected high value of $|\theta|$ and, in addition, T_N is almost constant for $x \geqslant 2/3$.

Magnetic properties of $SrFeO_{2.96}$ are quite peculiar because it shows the largest paramagnetic signal in spite of the absence of paramagnetic Gd^{3+}. In addition, $\chi'(T)$ does not obey the Curie–Weiss law in a broad temperature range. Fitting the data above 220 K, we obtain a value of $6.5\mu_B$ for the effective paramagnetic moment, which is much higher than the spin only value of $4.99\mu_B$ (92% of Fe^{4+} + 8% of Fe^{3+}). However, it agrees with values reported previously for this compound [7]. In addition, the fit yields a positive Weiss constant what might be related to the presence of ferromagnetic interactions in the paramagnetic state. This would also explain the large value of the paramagnetic susceptibility in this sample. Below T_N, the real component of $SrFeO_{2.96}$ susceptibility shows an anomaly at ~50 K, which corresponds to an increase of the out-of-phase component (not shown here). These features can be related to the onset of magnetic irreversibility and negative magnetoresistance [34]. They were explained in terms of a spin reorientation in the helical structure [35].

3.5. Current transport properties

The resistivity (ρ) of all $x \geqslant 2/3$ samples follows a semiconducting behavior. In Fig. 6 we have plotted the resistivity as a function of temperature for the nearly

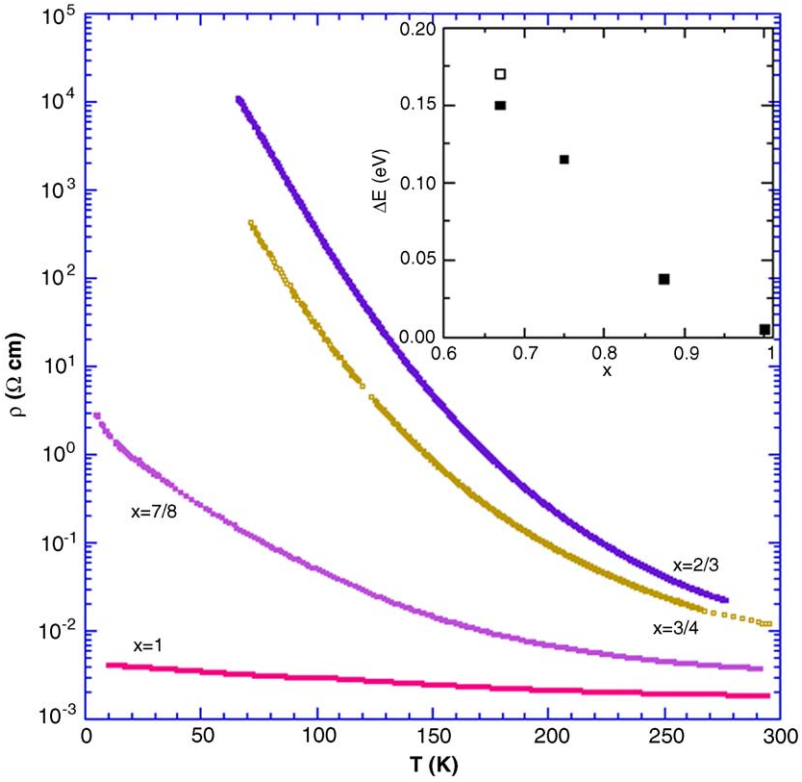

Fig. 6. Resistivity versus temperature for several $Gd_{1-x}Sr_xFeO_{3-\delta}$ samples. The inset shows the activation energy versus x. Solid squares stand for oxidized samples and open square stands for $Gd_{1/3}Sr_{2/3}FeO_{2.90}$.

stoichiometric samples. Resistivity increases as the Gd content increases. The experimental data at high temperatures (between 140 and 300 K) can be fitted to an Arrhenius law, $\rho = \rho_0 \exp(E_A/k_B T)$, where E_A and k_B are the activation energy and Boltzamnn's constant, respectively. The values of E_A obtained from the fits are shown in the inset of Fig. 6.

$SrFeO_{2.96}$ has the highest electrical conductivity in the series and the E_A for this compound is very small (~5 meV) suggesting that this composition is close to the metal–insulator boundary of the system. At low temperatures (~50 K) we have observed a broad anomaly with thermal hysteresis in the resistivity of this compound (not shown here), corresponding to the spin reorientation as discussed above [34,35].

The activation energy increases as the content of Gd or oxygen vacancies increases. It is clear that the rise of the Fe^{3+} concentration seems to be detrimental for the electronic conduction. Such behavior has been found in the $La_{1-x}Sr_xFeO_{3-\delta}$ system [15]. However, the conductivity of $Gd_{1-x}Sr_xFeO_{3-\delta}$ samples is smaller than that of $La_{1-x}Sr_xFeO_{3-\delta}$ system due to the lattice strains induced by the small size of Gd^{3+} ions. We have also determined the type of majority carriers for all samples at room temperature and at 77 K. The samples show n-type conductivity except for $Gd_{1/4}Sr_{3/4}FeO_{2.88}$ and $Gd_{1/3}Sr_{2/3}FeO_{2.90}$, which are p-type.

In order to gain insight into the conduction mechanisms, we have plotted $\ln \rho$ as a function of inverse temperature in Fig. 7. The activation energy in $Gd_{1/8}Sr_{7/8}FeO_{2.95}$ and $SrFeO_{2.96}$ decreases as temperature decreases. The low-temperature resistivity for $x<7/8$ samples is too high to be measured reliably but the overall trend is the same. The strong drop in E_A at temperatures between 50 and 100 K resembles the impurity conduction observed in compensated semiconductors at very low temperature [36]. Here, oxygen vacancies act as donor centers and the two extra-electrons left by each missing oxygen are located on the two Fe^{4+} sites (transforming into Fe^{3+}) adjacent to the empty oxygen site which act as acceptors. In Gd-compounds, an additional localization can occur due to the formation of Gd^{3+}–Fe^{3+} complexes which are energetically favorable. It is possible that some Fe^{3+} ions would be linked to neighbor Gd^{3+} ions. Therefore, the conduction through impurity states should be dominant at low temperature and ρ is best described by the expression of Mott's variable range hopping (VRH) for impurity conduction [37]: $\rho = \rho_0 \exp(A/T)^{1/4}$ with $A = W_D(\alpha R)^3 k_B^{-1}$. Here, W_D is the energy difference between localized states arising from disorder, α is the inverse localization length of the hydrogenic wavefunction describing the localized state and R is the mean distance between acceptor centers. The inset of Fig. 7 shows $\ln \rho$ versus $1/T^{1/4}$ plots for $Gd_{1/8}Sr_{7/8}FeO_{2.95}$ and $SrFeO_{2.96}$ samples. These curves are linear below 15–17 K as for conduction in the VRH regime. The linear fits yield $A = 5.23$ and $0.31\,K^{1/4}$ for $Gd_{1/8}Sr_{7/8}FeO_{2.95}$ and $SrFeO_{2.96}$, respectively. R can be taken as the interatomic average spacing between the acceptors.

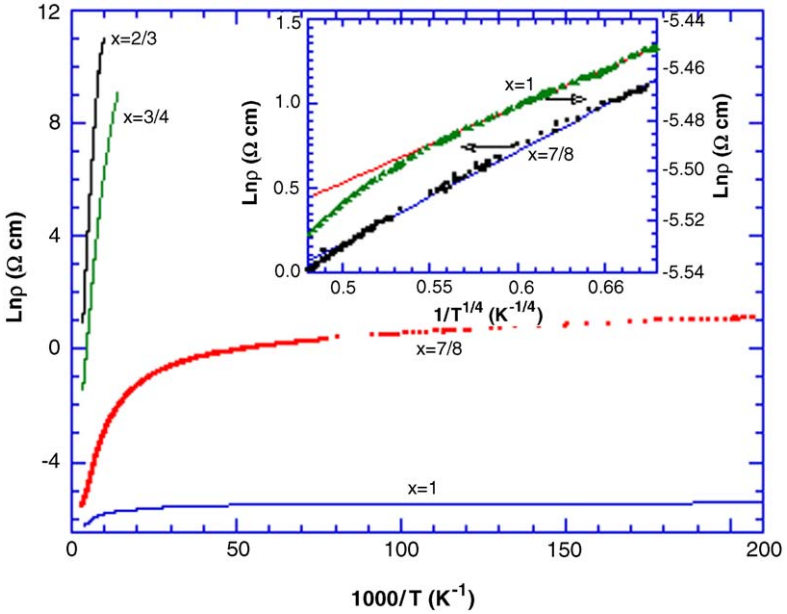

Fig. 7. Natural logarithm of resistivity versus $1000/T$ for the same samples of Fig. 6. Inset: $\ln\rho$ versus $1/T^{1/4}$ for $SrFeO_{2.96}$ and $Gd_{1/8}Sr_{7/8}FeO_{2.95}$. Linear fits for $T<15$ K are also shown.

Hence, $R=(2\times N_V)^{-1/3}$, where N_V is the number of oxygen vacancies per volume unit. Approximating the localization length as $\alpha^{-1}=\frac{1}{2}R(\pi/6)^{1/3}$ [38], we got for W_D the value of 4 meV in $Gd_{1/8}Sr_{7/8}FeO_{2.95}$. The activation energy is nearly zero for $SrFeO_{2.96}$ and it becomes larger upon increasing the Gd content probably due to the formation of Gd–Fe complex.

4. Discussion

The results obtained for $Gd_{1-x}Sr_xFeO_{3-\delta}$ allow us to see the role heavy rare-earths play in the properties of ferrites. We find that the single-phase solid solution does not exist for all values of x, contrary to the earlier reports [21]. A miscibility gap occurs between $x\sim0.09$ and 0.63. This sort of phase segregation is not new in the ferrite systems. It has been already described for related series such as $La_{1-x}Ba_xFeO_3$ [39]. For Gd system, the miscibility gap might arise from the size mismatch between Gd^{3+} and Sr^{2+} ions whose radii in a nine-fold coordination are 1.107 and 1.31 Å, respectively [26]. The Gd-rich samples show a strongly distorted orthorhombic cell since Gd^{3+} ion is too small for a 12-fold coordination. The Sr-rich samples however crystallize in a cubic structure with Sr^{2+} ion coordinated to 12 oxygen atoms. Then, phase segregation at intermediate compositions is a way to relax structural strains.

Ionic size mismatch leads to other phenomena in addition to phase segregation. Sr-rich samples are found to be all oxygen-deficient in spite of high-oxygen pressure treatment. This is another way to relief strain. We have checked that La-based compounds synthesized under the same conditions are oxygen stoichiometric for $x\leqslant3/4$. Lack of full oxygen stoichiometry in $RE_{1-x}Sr_xFeO_{3-\delta}$ systems with heavy rare-earth atoms affects significantly their physical properties. For instance, a rhombohedral unit cell has been reported for $La_{1-x}Sr_xFeO_3$ ($x=0.6$ and 0.7) [18] and for various $RE_{1/3}Sr_{2/3}FeO_3$ [12]. These authors also report a rhombohedral cell for the Gd-based sample contrary to our results. We have tried to index the X-ray patterns of $Gd_{1/3}Sr_{2/3}FeO_{2.96}$ using a rhombohedral unit cell that belongs to the $R\bar{3}c$ space group and the tilting scheme is $a^-a^-a^-$. At the first glance, the refinement seems to be good but this model fails to account for the splitting of some peaks in the high angle region. Therefore, the large size difference of the atoms occupying the 12-fold coordination sites favors the *Ibmm* cell.

It is worthwhile the comparison between $Gd_{1/3}Sr_{2/3}FeO_{2.90}$ and $SrFeO_{2.88}$. The former has a cubic cell indicating that oxygen vacancies are randomly distributed in the lattice. $SrFeO_{2.88}$ synthesized under the same conditions crystallizes in a tetragonal structure, which results from the long-range ordering of oxygen vacancies. Microdomains smaller than ~60 Å showing vacancy ordering cannot be discarded for $Gd_{1/3}Sr_{2/3}FeO_{2.90}$ (or $Gd_{1/4}Sr_{3/4}FeO_{2.87}$). Electron microscopy in addition to an electron diffraction study would be desirable at this point. In any case, the range of oxygen vacancies ordering depends also on the Gd/Sr size mismatch.

We have found that the Sr-rich $Gd_{1-x}Sr_xFeO_{3-\delta}$ compounds order at relatively low T_N, which varies only slightly with x. In the $La_{1-x}Sr_xFeO_3$ system however, T_N decreases as x (or nominal Fe^{3+} concentration) increases [11,15]. Above T_N, the susceptibility variation in $Gd_{1-x}Sr_xFeO_{3-\delta}$ ($2/3\leqslant x<1$) system obeys the Curie–Weiss law. The obtained effective paramagnetic moments reasonably agree with the sum of contributions expected from Gd and Fe ions. Both kinds of Fe ions are in high

spin state, in agreement with spectroscopic results [10]. Curiously, the highest paramagnetic signal is found in $SrFeO_{2.96}$, the compound without rare-earth ion. This finding points out to the presence of ferromagnetic correlations in the paramagnetic region [34].

The Sr-rich compounds are semiconducting in the whole temperature range studied. At high temperature, the resistivity follows an activated behavior whose activation energy ranges between 5 and 180 meV (see inset Fig. 6). These values are too small for an intrinsic gap transition since $REFeO_3$ compounds have a charge transfer gap of around 2 eV whereas stoichiometric $SrFeO_3$ is metallic. Moreover, the type of carriers changes from n to p when the formal content of Fe^{3+} increases. Such behavior was also observed in the $La_{1-x}Sr_xFeO_{3-\delta}$ series for a Fe^{4+} content close to 35% [15] or 50% [11]. In our $Gd_{1-x}Sr_xFeO_{3-\delta}$ samples, the change in the type of carriers occurs between $Gd_{1/3}Sr_{2/3}FeO_{2.96}$ (59% of Fe^{4+} and n-type) and $Gd_{1/4}Sr_{3/4}FeO_{2.88}$ (49% of Fe^{4+} and p-type). A model assuming that only octahedral irons contribute to the conductivity [11,15] may account for such behavior. The carriers are holes when octahedral Fe^{3+} are majority ions whereas n-type conductivity in a narrow e_g band takes place when octahedral Fe^{4+} are in majority. It is assumed that holes mainly goes to Fe 3*d* bands for low Sr content, contrary to spectroscopic findings [10].

It is very likely that Fe^{4+} exhibits a strong covalency with surrounding oxygen ions. This will give rise to a conduction band formed by Fe-3$d(e_g)$ and O-2*p* orbitals. The Fermi energy, E_F, would be in this band for stoichiometric $SrFeO_3$. The electronic configuration for iron ions would be $3d^4+3d^5L$. Oxygen vacancies introduce disorder. Consequently, a mobility edge (E_C) can appear over the E_F. The electron transport occurs via activation of carriers to E_C with a relative small $E_A=E_C-E_F$ (Anderson transition). The addition of Gd^{3+} increases the local disorder leading to an increase of E_A.

Both covalency and Fe 3*d*–O 2*p* states mixing diminish for a large Fe^{3+} content. E_F level lies in the top of oxygen 2*p* band as expected for a doped charge transfer insulator [10]. The conductivity is then by hole hopping in this band.

5. Concluding remarks

We have studied the $Gd_{1-x}Sr_xFeO_{3-\delta}$ series synthesized using high oxygen pressure. Our study shows that the Gd/Sr size mismatch induces a structural strain that leads to phase separation between $x\sim0.09$ and 0.63. Then, the two phases region is centered at $x\sim0.36$ with a width of $\Delta x\sim0.54$. It would be interesting to see how these parameters vary with the *RE* size, i.e., whether Δx continuously tends to zero with increasing *RE* size ($\Delta x\sim0$ for La and Pr-based compounds according to Refs. [18,19]) or whether there is a critical size for the phase separation in the whole range.

The crystal structure for $x<0.09$ is $GdFeO_3$-type with a strong orthorhombic distortion. The Sr-rich compounds however, show cubic or nearly cubic structures. Here, the structural strain is relieved by either oxygen vacancies or FeO_6 octahedra tilting. The long-range ordering of oxygen vacancies observed for $SrFeO_{2.88}$ [16] disappears upon substituting Gd for Sr. On the other hand, we find that $Gd_{2/3}Sr_{1/3}FeO_{2.90}$ crystallizes in the *Ibmm* space group giving rise to a new allotype in the field of orthoferrites.

$Gd_{1-x}Sr_xFeO_{3-\delta}$ ($x\geqslant2/3$) compounds order antiferromagnetically at low temperature with a minimum T_N of 72 K for $x=7/8$. Above T_N, their susceptibilities obey the Curie–Weiss law except for $SrFeO_{2.96}$, which exhibits a strong paramagnetic signal indicating ferromagnetic correlations.

There is a change in the type of conduction as the Gd doping increases. The conductivity of n-type indicates a strong Fe 3*d*–O 2*p* mixing at the Fermi level and is observed for a Fe^{3+} content $\leqslant41\%$ in our samples. For higher Fe^{3+} content ($\geqslant51\%$), the Fe–O covalency diminishes and the Fermi level lies in the O 2*p* band, with p-type conduction. This interpretation is in agreement with previous spectroscopic results [10]. Finally, the transport properties for n-type compounds agree with the occurrence of an Anderson transition due to atomic disorder. The conductivity is activated at high temperature with a small activation energy that increases as disorder (vacancies or Gd content) increases. This corresponds to the rise in the difference between mobility edge and Fermi level with increasing content of Fe^{3+}. At low temperature, the conduction mechanism is a variable range hopping between localized states.

Acknowledgments

Financial support from CICyT (projects MAT02-01221 and MAT02-166) and DGA (CAMRADS group) are acknowledged. We are indebted to M. C. Sánchez and Servicio Nacional EXAFS of Zaragoza University for the acquisition of X-ray patterns.

References

[1] J.A. Bahteeva, I.A. Leonidov, M.V. Patrakeer, et al., J. Solid State Electrochem. 8 (2004) 578–584.
[2] J.Q. Li, Y. Matsui, S.K. Park, Y. Tokura, Phys. Rev. Lett. 79 (1997) 297–300;
M. Takano, J. Kawachi, N. Nakanishi, Y. Takeda, J. Solid State Chem. 39 (1981) 75–84.
[3] T. Akao, Y. Axuma, M. Usuda, Y. Nishihata, J. Mizuki, N. Hamada, H. Hayashi, T. Terashima, M. Takano, Phys. Rev. Lett. 91 (2003) 156405.
[4] J. Matsuno, T. Mizokawa, A. Fujimori, Y. Takeda, S. Kawasaki, M. Takano, Phys. Rev. B 66 (2002) 193103.
[5] M. Marezio, J.P. Remeika, P.D. Dernier, Acta Crystallogr. B 26 (1970) 2008.
[6] M. Eibschütz, S. Shtrikman, D. Treves, Phys. Rev. 156 (1967) 562.
[7] J.B. MacChesney, R.C. Sherwood, J.F. Potter, J. Chem. Phys. 43 (1965) 1907–1913.
[8] T. Takeda, Y. Yamaguchi, H. Watanabe, J. Phys. Soc. Japan 33 (1972) 967.

[9] T. Takeda, S. Komura, H. Fujii, J. Magn. Magn. Mater. 31 (1983) 797–798.
[10] M. Abbate, F.M.F. de Groot, J.C. Fuggle, A. Fujimori, O. Strebel, F. Lopez, M. Domke, G. Kaindl, G.A. Sawatzky, M. Takano, Y. Takeda, H. Eisaki, S. Uchida, Phys. Rev. B 46 (1992) 4511.
[11] A. Wattiaux, J.C. Grenier, M. Pouchard, P. Hagenmuller, J. Electrochem. Soc. 134 (1987) 1718–1724.
[12] T. Ishikawa, S.K. Park, T. Katsufuji, T. Arima, Y. Tokura, Phys. Rev. B 58 (1998) R13326–R13329.
[13] P.D. Battle, T.C. Gibb, P. Lightfoot, J. Solid State Chem. 84 (1999) 271–279.
[14] S.K. Park, T. Ishikawa, Y. Tokura, J.Q. Li, Y. Matsui, Phys. Rev. B 60 (1999) 10788–10795.
[15] J.C. Grenier, N. Ea, M. Pouchard, M.M. Abou-Sekkina, Mater. Res. Bull. 19 (1984) 1301–1309.
[16] J.P. Hodges, S. Short, J.D. Jorgensen, X. Xiong, B. Dabrowski, S.M. Mini, C.W. Kimball, J. Solid State Chem. 151 (2000) 190–209.
[17] M.A. Alario-Franco, M.J.R. Henche, M. Vallet, J.M.G. Calbet, J.C. Grenier, A. Wattiaux, P. Hagenmuller, J. Solid State Chem. 46 (1983) 23–40.
[18] S.E. Dann, D.B. Currie, M.T. Weller, M.F. Thomas, A.D. Al-Rawwas, J. Solid State Chem. 109 (1994) 134–144.
[19] H.W. Brinks, H. Fjellvåg, A. Kjekshsus, B.C. Hauback, J. Solid State Chem. 150 (2000) 233–249.
[20] C.S. Kim, Y.R. Um, S.I. Park, S.H. Ji, Y.J. Oh, J.Y. Park, S.J. Lee, C.H. Yo, IEEE Trans. Magn. 30 (1994) 4918–4920.
[21] C.H. Yo, E.S. Lee, M.S. Pyon, J. Solid State Chem. 73 (1988) 411–417.
[22] J. Rodríguez-Carvajal, Physica B 192 (1992) 55–69, Available at www-llb.cea.fr
[23] P. Karen, P. Woodward, J. Mater. Chem. 9 (1999) 789–797.
[24] M. Karppinen, M. Matvejeff, K. Salomäki, H. Yamauchi, J. Mater. Chem. 12 (2002) 1761–1764.
[25] A.M. Glazer, Acta Crystallogr. A 31 (1975) 756–762.
[26] R.D. Shannon, Acta. Crystallogr. A 32 (1976) 751–767.
[27] P.M. Woodward, Acta Crystallogr. B 53 (1997) 32–43.
[28] V.M. Goldschmidt, Naturwissenschaften 14 (1926) 477–485.
[29] P.M. Woodward, Acta Crystallogr. B 53 (1997) 44–46.
[30] P.G. Radaelli, M. Marezio, H.Y. Hwang, S.-W. Cheong, J. Solid State Chem. 122 (1996) 444–447.
[31] V. Caignaert, F. Millange, M. Hervieu, E. Suard, B. Raveau, Solid State Commun. 99 (1996) 173–177.
[32] D.T. Marx, P.G. Radaelli, J.D. Jorgensen, R.L. Hitterman, D.G. Hinks, S. Pei, B. Daborwski, Phys. Rev. B 46 (1992) 1144–1156.
[33] T. Maeder, J.G. Bednorz, J. Eur. Ceram. Soc. 19 (1999) 1507–1510.
[34] Y.M. Zhao, P.F. Zhou, J. Magn. Magn. Mater. 281 (2004) 214–220.
[35] A. Lebon, P. Adler, C. Bernhard, A.V. Boris, A.V. Pimenov, A. Maljuk, C.T. Lin, C. Ulrich, B. Keimer, Phys. Rev. Lett. 92 (2004) 037202.
[36] A.J. Springthorpe, I.G. Austin, B.A. Austin, Solid State Commun. 3 (1965) 143.
[37] I.G. Austin, N.F. Mott, Adv. Phys. 18 (1969) 41–102.
[38] V.N. Bogolomov, E.K. Kudinov, Y.A. Firsov, Sov. Phys. Solid State 9 (1988) 2502.
[39] J. Li, J. Jing, J. Mater. Sci. 27 (1992) 4361–4364.